Discrete element modeling of strongly deformed particles in dense shear flows

Powder Technology 401 (2022) 117288

Contents lists available at ScienceDirect

Powder Technology

journal homepage: www.elsevier.com/locate/powtec

Discrete element modeling of strongly deformed particles in dense shear flows

Nazanin Ghods [a,*], Payam Poorsolhjouy [b], Marcial Gonzalez [c,d], Stefan Radl [a]

[a] Institute of Process and Particle Engineering, Graz University of Technology, Inffeldgasse 13/III, 8010 Graz, Austria
[b] Department of the Built Environment, Eindhoven University of Technology, 5612, AZ, Eindhoven, Netherlands
[c] School of Mechanical Engineering, Purdue University, West Lafayette, IN 47907, USA
[d] Ray W. Herrick Laboratories, Purdue University, West Lafayette, IN 47907, USA

ARTICLE INFO

Article history:
Received 20 December 2021
Received in revised form 10 March 2022
Accepted 11 March 2022
Available online 15 March 2022

Keywords:
Discrete element method
Simple shear flow
Deformable particles
Response surfaces

ABSTRACT

The discrete element method (DEM) proposed by Cundall and Strack [1] is a widely used numerical approach to study the fundamentals of particulate matter at the particle scale. In our present study, the flow behavior of dense configurations of soft particles was studied by means of a new formulation of the multi-contact force closure for the DEM. The first step was to verify the response of the new force closure, and calibrate its parameters based on a comparison of the results for simple uniaxial compression with results from a reference simulation. This reference simulation used a highly accurate nonlocal formulation of contact mechanics in the quasi-static limit [2], which accounts for the interplay of deformations due to multiple contact forces acting on a single particle. The newly developed and calibrated model results show significant improvement over those derived via the existing multi-contact model. Also, the dependence of the stress in the sheared granular matter on the Poisson's ratio was unveiled when using the newly derived advanced multi-contact force closure. Therefore, an extensive campaign of simple shear flow simulations was performed (at a fixed volume of the simulation box) to probe the effect of particle volume fraction and the speed of shearing. These simulations show that the stress at particle volume fractions larger than a critical value depends not only on the friction coefficient and particle stiffness, but also on the Poisson's ratio of the material. Finally, we report a response surface for the pressure in a sheared particle bed as a function of all key influence parameters. This response surface is beneficial for calibrating DEM model parameters in extremely dense flow configurations.

1. Introduction

Soft solid or fluid particles, including gels, rubber, powders, clays, microorganisms, cells, droplets, bubbles, etc., are encountered in many applications from food to bio-medical industries. The deformability of soft particles is vital for understanding their bulk and mechanical behavior as it is a key characteristic in many manufacturing steps, such as separation and purification.

In numerical simulations of these systems, only small deformations of the involved particles are typically considered. Thus, particles are either treated as rigid bodies (e.g., in the case of the hard-sphere method), or deformations are idealized (e.g., in the case of the DEM). Despite this, an investigation of large deformations is essential, e.g., for a better understanding of many industrial processes such as (i) tableting and granulation processes in the food and pharmaceutical industry [3], (ii) investigations of the outflow dynamics and clogging during silo discharge [4], or (iii) biomedical applications, for instance, studying the flow properties of blood cells [5].

The discrete element method (DEM) [1] is a powerful numerical method for modeling and analysis of the behavior of various particulate systems [6–9]. The particles in DEM interact with each other via pairwise contact forces. Employing the usual soft-particle approach, which assumes a tiny overlap of particles corresponding to the particle deformation at the contact point, particles can stay in contact for a finite amount of time. Although multiple contact forces are allowed to act on a particle in this approach, each interparticle contact is usually considered binary and independent of other contacts. We denote such an approach as "classical DEM" since it reflects the original idea of Cundall and Strack [1]. However, the assumption of independent contacts is only valid for moderately dense granular systems in which deformations are small and localized around the contact point. Therefore, the classic DEM is imperfect for modeling ensembles of particles that undergo large deformations.

One common way of introducing deformability is by combining the capabilities of the finite element method (FEM) with DEM [10–14] by

* Corresponding author.
E-mail address: nghods@tugraz.at (N. Ghods).

https://doi.org/10.1016/j.powtec.2022.117288

discretizing individual particles. Although pure FEM can also be used for accurate particle deformation modeling, the method is mesh-dependent, computationally expensive, and limited to account for large deformations [11]. Other discretization methods, such as the continuum-based material point method [15–17] or the discrete-bonded particle method [18], have also been introduced for this purpose. Although these methods are beneficial in modeling different deformation mechanisms and any particle shape, they are computationally costly and suitable only for a limited number of particles.

Other complex methods have been introduced to consider the deformability in DEM. One is the deformable discrete element method (DDEM) [19], where particles are deformed uniformly due to consistent internal stress. In DDEM, the strain created inside of each particle (i.e., a so-called "local strain") affects the evaluation of binary contact forces by using newly formed global overlaps (i.e., so-called "global strains"). DDEM was developed for disks and is applicable to 2D situations only [19]. Another method is discrete deformation analysis (DDA), developed by Shi [20], which employs an implicit solution algorithm demanding the evaluation of stiffness matrices of deformable blocks. These formulations were developed for deformable cylindrical (in 2D) and deformable blocks, respectively. What hinders using these methods is that they are relatively complex for even simple 2D modeling, and further developments are needed for 3D applications.

An interesting method called the multi-contact DEM (MC-DEM) was first developed by Brodu et al. [21]. This method explicitly considers the mutual influence of the formation of new contacts due to the particles' deformation to evaluate the contact force. In this model, the deformation is employed by an analytical solution. Brodu et al. have successfully compared the results of their MC-DEM model with experimental data of uniaxial compression of hydrogel particles. Recently, Giannis et al. [22] have introduced a stress-based MC-DEM variant. Specifically, they use the trace of the particle stress tensor in order to consider the simultaneous effect of all contacts on a single particle. This MC-DEM variant has been validated by confined and unconfined uniaxial compression of different materials like hydrogels, rubber, and glass beads. Giannis et al. [22] have shown that their stress-based MC-DEM model is computationally much faster than methods involving particle discretization.

Granular materials exhibit a flow behavior that ranges from that of a gas to that of a solid, depending on their properties and the interaction between grains. In dense flows above the critical (jamming) solid volume fraction, the effect of the formation of new contacts and a realistic evaluation of contact forces is of significant importance. Despite the advantages mentioned above of the MC-DEM method, this model is numerically not capable of simulating the extremely dense configuration of strongly deformed particles. Specifically, our preliminary analysis shows that employing standard MC-DEM for large deformations can lead to situations where the corrected contact surfaces predicted by the model are extremely huge (data not shown). This behavior results in contact penetrations larger than the particle's radius. This is physically impossible and hence needs to be corrected.

In our current study, the standard MC-DEM model has been improved to be capable of modeling extremely dense configurations of highly deformable particles that standard MC-DEM cannot cover. This advanced MC-DEM method is ultimately employed to investigate simple shear flows beyond the jamming point. Due to the computational efficiency of contact detection and the simplicity of implementation, spherical particles are often preferred and the focus of our present study. Firstly, the verification of the proposed method and the calibration of the model parameters were carried out for uniaxial compression of granular matter, using the highly accurate nonlocal contact formulation of Gonzalez et al. [2,23,24]. Subsequently, a large set of simple shear flow simulations within the quasi-static regime was executed to investigate the effect of particle volume fraction and the shear rate on the time-averaged pressure. Lastly, considering the Poisson's ratio effect, a response surface for the pressure in this regime is presented as a function of all key parameters. That is of value for the calibration of parameters in future applications of our model.

2. Simulation approach and computational model

Simulations are performed using the discrete element method (DEM) solver LIGGGHTS [25]. The DEM includes solving Newton's equations for every particle's translational and angular momentum [1]. Grains are modeled as inelastic, frictional spheres, interacting through a modified Hertz's law. Specifically, an advanced multi-contact surface model, which is capable of modeling dense configuration of soft particles and explained in the next paragraph, is used to improve Hertz's law for binary contact forces.

Brodu et al. [21] has first introduced the standard multi-contact (MC) model. This model considers the influence of induced deformations at neighboring contact points when calculating particle-particle contact forces.

In the classical DEM method, contact laws relate the contact force to the overlap of two particles. If two particles i and j, with radii r_i and r_j and positions x_i and x_j are in contact, this overlap is:

$$\delta_c = (r_i + r_j) - (\mathbf{x}_i - \mathbf{x}_j) \cdot \mathbf{n} \tag{1}$$

where $\mathbf{n}$ is the unit vector pointing from particle j to i.

In MC-DEM based models, the displacement field imposed by neighboring contacts $\delta_{k\to c}$ (k denotes here the neighbour contact index) at each local contact δ_c is calculated by the following expression derived by elasticity theory [21]:

$$\delta_{k\to c} = -\gamma \frac{(1+\upsilon)F_k}{2\pi E d_{kc}} \left\{ (\mathbf{n}_k \cdot \mathbf{u}_{kc})(\mathbf{n}_c \cdot \mathbf{u}_{kc}) + (3-4\upsilon)\mathbf{n}_k \cdot \mathbf{n}_c - (1-2\upsilon)\frac{(\mathbf{n}_k + \mathbf{u}_{kc}) \cdot \mathbf{n}_c}{1 + \mathbf{n}_k \cdot \mathbf{u}_{kc}} \right\} \tag{2}$$

where F_k is the force at contact k, $\mathbf{n}_k$ is a surface normal vector at contact point k, $\mathbf{u}_{kc}$ is the unit vector connecting the contact point k to c, E is the Young's modulus of the particles, d_{kc} is the distance between the surface position of contacts c and k, υ is the Poison's ratio, and γ is an adjustable pre-factor that empirically accounts for the geometry. Consequently, the contact force will be defined as some function f of $(\delta_c + \sum_k \delta_{k\to c})$ instead of δ_c as done in the classical DEM. For instance, using the Hertzian contact law, the contact force will be proportional to $(\delta_c + \sum_k \delta_{k\to c})^{3/2}$. Based on the relative distance of the two contact surface positions c and k and the Poisson's ratio, the evaluated value of the terms in the curly brackets in Eq. (2) can be negative or positive. Therefore, this solution considers the deformation of particles as if the particles' radius is reduced or increased for contact force detection and evaluation. Furthermore, this method assumes that the deformation is isotropic enough such that there is no need to recompute the moment of inertia tensor of each grain after deformations.

Deploying the standard MC-DEM for modeling large deformations is beneficial in closely packed situations. Unfortunately, the corrected contact surface positions resulting from applying the above-mentioned displacement field for extreme conditions can lead to negative overlaps (i.e., the particles' contact position passes each other's centers). This is clearly unphysical.

To address this problem, we propose a modification to this method in a way that (for each contact) the displacement field caused by each neighboring contact (as given by Eq. 2) is limited to a maximum penetration ratio, $MPR = \delta_{max}/r_i$, where r_i is the particle's i radius. This means that Eq. (2) is only effective for contact overlaps that are less than the allowed MPR multiplied by the particle radius. MPR signifies the ratio

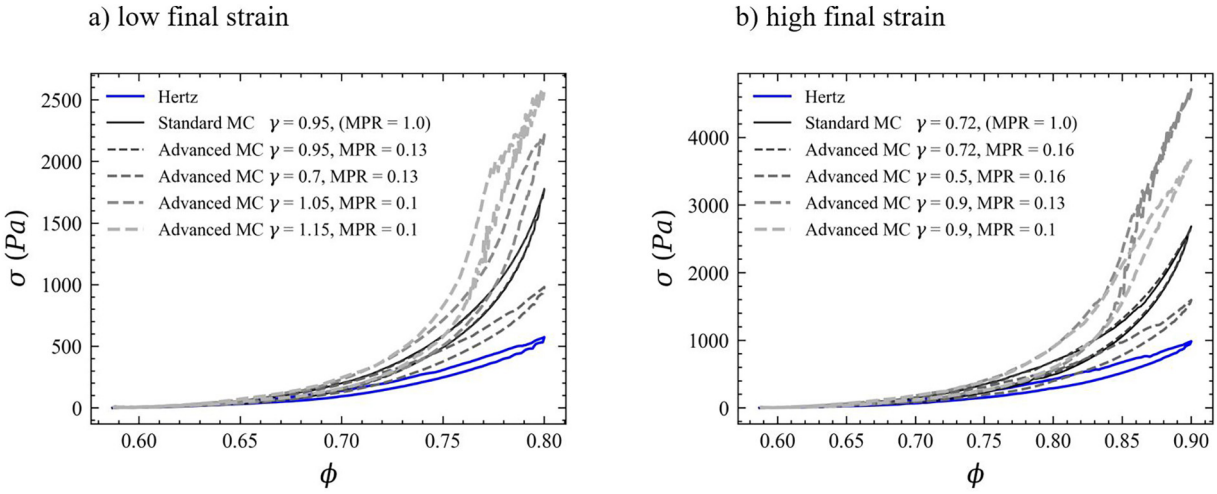

Fig. 1. Normal stress acting on the top plate during compression and decompression of hydrogel particles up to two final strain levels (panel a: low strain, panel b: high strain) versus solid volume fraction of the bed. Classical DEM with Hertzian contact force (solid blue line), standard MC (solid black line), and advanced MC model with different sets of model parameters (dashed lines).

between the maximum displacement per contact δ_{max} and the radius of the particle. Thus, the contact force is redefined as:

$$F_k = \begin{cases} f(\delta_c) & if \quad \delta_{k\to c} > \delta_{max} \\ f\left(\delta_c + \sum_k \delta_{k\to c}\right) & if \quad \delta_{k\to c} \le \delta_{max} \end{cases} \tag{3}$$

For displacements above the defined maximum, the deformation at each contact is so large that standard multi-contact (MC) equations would lead to numerical instabilities. Thus, one needs to choose an expression that leads to a stable (and realistic) contact force, which we find is satisfied by the base contact law (i.e., the Hertz law).

It has to be noted that the *overlap* (or *deformation* and *penetration ratio*) terms used in the model's description are only referring to the DEM contact force calculation as the soft-sphere approach. Thus, the extent of the overlap of particles relates to the magnitude of the contact force. In the MC-DEM, the particles neither change size nor are deformed. Moreover, the MC-DEM is a surface model approach for considering the effect of multiple contacts in contact detection and contact force calculation in DEM simulations, compatible with any contact law - the Hertz law is used in this study. In Appendix A we have illustrated the corresponding computer algorithm of the advanced multi-contact model. Therefore, MPR = 0 relates to binary contact calculation and detection, while MPR = 1 resembles multiple contact calculation for all the contacts. In this research, we discovered that since the displacement field imposed by neighboring contacts (Eq. 2) approximates the particulate packing to an infinite half-space, small overlaps adding the effect of other contacts can be more important than a large overlap. In the standard MC closure, the addition of this approximation for large overlaps provoked large deviations in the displacement field prediction, resulting in unphysical results.

The MPR value and the empirical pre-factor (γ) need to be calibrated for a given assembly when using the advanced MC closure. In what follows, the calibration strategy and how switching back to the Hertz solution results in stable and realistic results is discussed.

3. Verification and calibration

The advanced MC-DEM model has two parameters that should be calibrated and that are dependent on the particle properties. Therefore, the uniaxial compression test case of hydrogel particles by Brodu et al. [21] was replicated. This setup allows the study of extreme compaction conditions (i.e., reaching solid volume fractions of 0.85). We used our advanced and the standard multi-contact model of Brodu et al. [21] to simulate it. The system contains 514 hydrogel particles with a mean diameter of 2.1 ± 0.2 [*cm*], packed into a rectangular bed with the initial size of 0.165 × 0.166 × 0.168 [m] in x-y-z direction (further particle properties are summarized in Appendix B). The initial solid volume fraction of the bed of particles is 0.58. The particles are uniaxially compressed and decompressed in the z direction with a constant velocity of 0.1 m/s. For all the simulations, the DEM timestep is chosen to be below the critical value [26], therefore ensuring stable simulations and the independence of the calibrated parameters to the chosen time step.

wAs is expected, our advanced MC-DEM predicts higher forces compared to the classical Hertz model (see Fig. 1). The solid black lines correspond to the standard MC-DEM prediction using the maximum γ pre-factor that is numerically reachable (i.e., without numerical failure).

The effect of the MPR is highly dependent on the number of contacts and the distribution of the overlap values within the system, and the contact force between particles. The reason is that if the contact force from the previous timestep is overestimated - this can happen with large γ factors - the contact model switches back to the base model

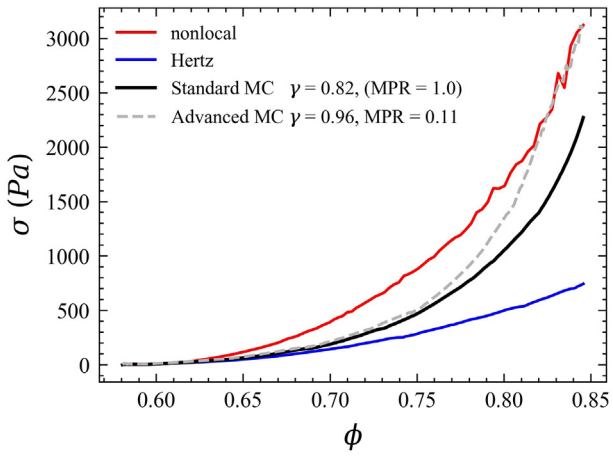

Fig. 2. Stress vs. solid volume fraction for the compression of hydrogel particles using the nonlocal formulation [2], classical DEM with Hertzian contact force, standard MC-DEM [21], and the advanced MC.

(i.e., the Hertz model). The results closely agree with the standard MC-DEM by decreasing the MPR from 1.0 to a particular value, depending on the final solid volume fraction (and the maximum overlaps). In turn, the results now rely on the value for γ (indicated as dashed grey lines in Fig. 1). Fortunately, when reducing the MPR value, the γ pre-factor can be increased to reach the desired stress levels.

The response of the advanced MC-DEM force closure with different pairs of parameters during the compression cycle is demonstrated in

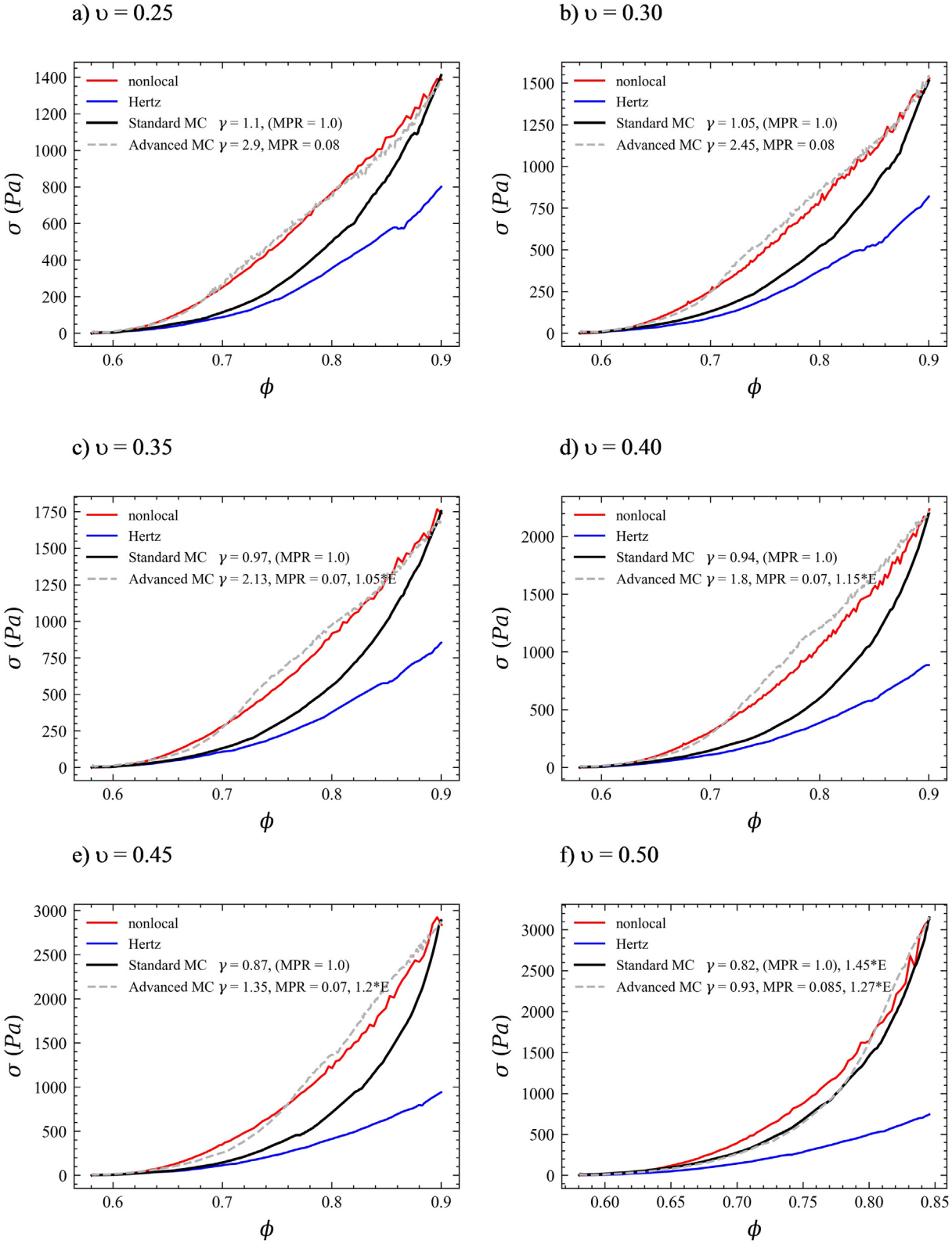

Fig. 3. Stress vs. solid volume fraction plot of compression case for the nonlocal formulation [2], classical DEM with Hertzian contact force, standard MC-DEM [21], and the advanced MC, for different Poisson's ratios.

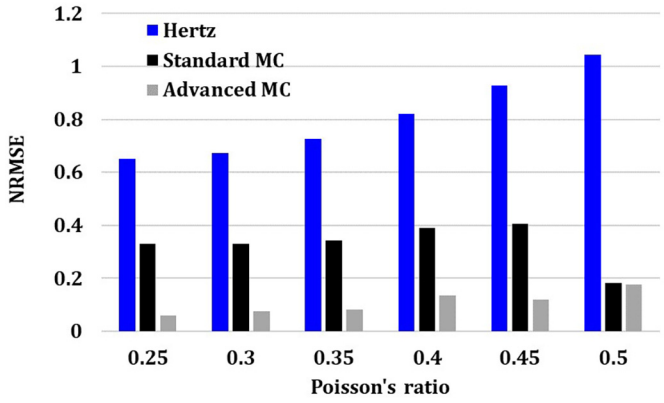

Fig. 4. The normalized root-mean-square error (NRMSE) of Hertz, Standard and advanced MC method relative to the reference results (i.e., the nonlocal formulation) for various Poisson's ratios.

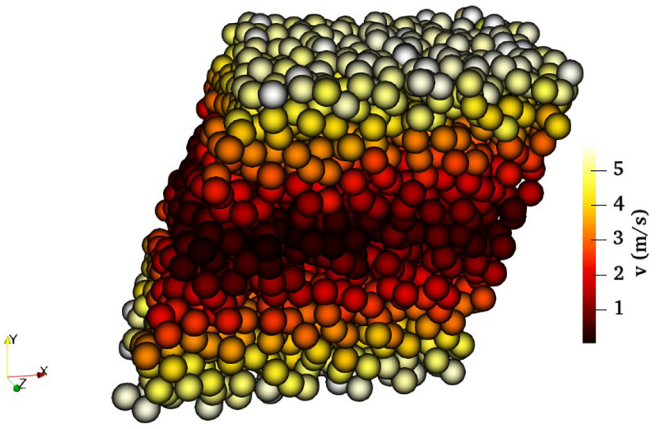

Fig. 6. Granular matter at a volume fraction of 0.9 in simple shear flow (colors indicate individual particle speed).

Fig. 1. The second compression-decompression cycle has been plotted to eliminate the effect of the packing's initial configuration, as well as the rearrangement of particles during the initial compression. This protocol was also adopted to make the response reversible and reach the initial packing fraction after decompression. The simulated stress response is consistent with similar compression experiments of deformable spheres such as hydrogel and rubber, where for the first 1–2 mm of displacement (corresponding to $\phi = 0.66$), the packing follows the Hertzian relationship, while at larger displacements (i.e., $\phi > 0.66$), a transition to a stiffer behavior is observed [27–30].

Our advanced multi-contact model predictions are validated by comparing with Gonzalez's nonlocal contact formulation [2] results in the quasi-static limit. The latter accounts for the interplay of deformations due to multiple contact forces acting on a single frictionless particle. Precisely, the effect of each contact load on every point of the particle's surface is estimated using a closed-form solution, which allows for an efficient formulation scheme to incorporate nonlocal effects. The above-mentioned uniaxial compression test case of hydrogel particles was simulated for the most extreme compaction conditions up to which the nonlocal formulation could handle (this was $\phi = 0.85$), and the results are shown in Fig. 2. Additional test cases for a single-particle, and a body-centered cubic arrangement of particles, are reported in Appendix B.

The standard MC model can be securely used for dilute systems (i.e., in a range around the critical solid volume fraction). Under high consolidation conditions, it is recommended to switch to the advanced MC method for stability reasons. It is observed that using the standard MC method, with the highest numerically-possible γ pre-factor (i.e., the critical γ pre-factor), the stress levels that are predicted by the nonlocal formulation cannot be reached. In contrast, reaching the high stress predicted by the nonlocal formulation is achievable by calibrating the advanced MC parameters. Unfortunately, as Fig. 2 shows, the exact σ versus ϕ path obtained with the nonlocal formulation cannot be replicated when using the advanced MC method.

This disadvantage can be removed when following a calibration approach in which Young's modulus in the MC approach is also considered a variable. Specifically, the idea is to increase the Young's modulus to capture better the slope of the σ versus ϕ path at intermediate volume fractions around $\phi = 0.7$. When following such an idea, Fig. 3a and Fig. 3b demonstrate that for low Poisson's ratios (i.e., $\nu \leq 0.30$), the results of the nonlocal formulation can be perfectly replicated by adjusting MPR and γ only. Thus, the additional complication of modifying the Youngs modulus is not necessary. Also, it can be observed that the standard MC cannot be changed to give satisfactory agreement for this range of Poisson's ratios.

Fig. 3c-f illustrate the results for $\nu > 0.30$. It is observed that although the standard MC shows a good performance for the highest Poisson's ratio investigated, the results of the advanced MC method necessitate a smaller increase of the Youngs modulus (see Fig. 3f). Therefore, compared to standard MC, the particles' stiffening (i.e., increase of E) will only slightly force the decrease of the simulation timestep. This finding becomes more significant when simulating a larger number of particles for which the time steps size directly affects simulation time. It has to be noted that, when increasing the stiffness, the analytical agreement at

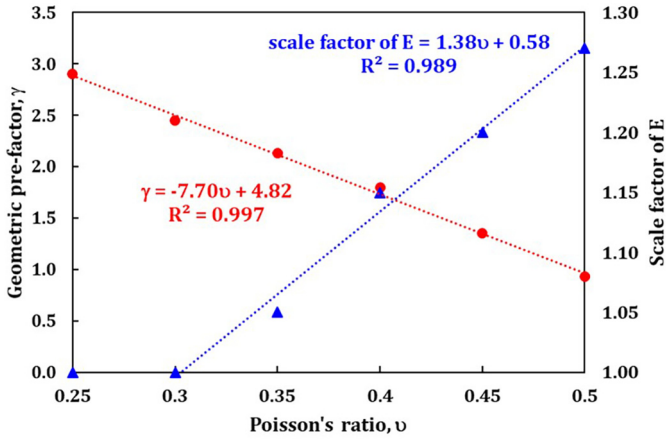

Fig. 5. Calibrated geometric pre-factor γ and E as a function of the Poisson's ratio.

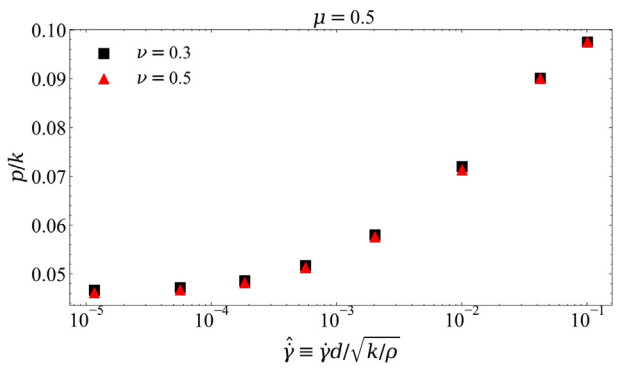

Fig. 7. Dimensionless pressure vs. dimensionless shear rate for two Poisson's ratios, using standard DEM and a Hertzian contact law ($\phi = 0.8$).

comparably dilute packings (only a few contacts per particle) will be lost. However, this is irrelevant for the stress levels of interest. Also, it is observed from Fig. 3f that as the particles' material approaches a Poisson's ratio of 0.5 (i.e., the material behaves incompressible), a greater stiffening is required.

For other Poisson's ratios (for results, see Fig. 3c-e), it was observed that the full σ versus ϕ path could only be replicated when using our advanced MC model. However, the final desired stress level can also be reached using the inferior standard MC model. In summary, the optimal geometric pre-factor γ in the standard MC method must be chosen as a function of the final packing fraction to match the nonlocal results. In contrast, there is more freedom in the advanced MC method since γ and the MPR value can be adjusted. Here we found that with low MPR values, not only the desired maximum compression pressure can be met, but the exact stress-strain path can also be obtained.

The normalized root-mean-square error NRMSE of the predictions, i.e., the RMSE value divided by the arithmetic average of the σ-ϕ data points of the nonlocal formulation calculations, are summarized in Fig. 4. It significantly improves the results when advancing from a simple Hertz force closure to our advanced MC closure. As the Poisson's ratio of the particles increases, the NRMSE increases as well.

Considering the calibrated parameters for the advanced MC method, one finds that the calibrated γ factor should linearly decrease with increasing Poisson's ratio, and for $\upsilon > 0.3$, the calibrated E should increase linearly with increasing Poisson's ratio (see Fig. 5). The MPR value seems to vary between 0.07 and 0.09. This observation facilitates the calibration procedure of the advanced MC method. It has to be noted that density did not affect the calibrated parameters, since the particle volume fraction and bulk density were considered to scale linearly with particle density.

4. Simple shear flow

4.1. Setup and postprocessing strategy

The MC force closure presented above becomes more relevant in situations where the formation of new contacts plays an important role. Thus, simulations of closely packed soft particles and conditions close to or above jamming should use a MC force closure. To investigate the predictive capabilities of MC force closures, a simple shear flow of assemblies of about $N = 2000$ monodispersed particles in a cubic periodic simulation box with Lees-Edward boundary condition [31] was studied. This setup leads to a perfect linear shear flow at all volume fractions, as illustrated in Fig. 6. An extensive set of simulations, all in jammed conditions beyond the random close packing limit, considering a time-invariant shear rate $\dot{\gamma}$ were performed. Specifically, packings with solid volume fractions of $\phi = 0.625, 0.65, 0.7, 0.75, 0.8, 0.85$ and 0.9 were studied. We ensured that the results were not affected by the finite size of the simulation box by running simulations involving up to ~20,000 particles.

The contact model parameters are set according to the study of Chialvo et al. [32]. The adjustable geometric pre-factor γ and the MPR value of the advanced multi-contact model were selected as a function of the Poisson's ratio, as discussed in the previous section.

Based on the particles' position and velocity, a macroscopic stress tensor is calculated as:

$$\sigma = \frac{1}{V}\sum_i \left[\sum_{j\neq i}\frac{1}{2}\mathbf{r}_{ij}\mathbf{F}_{ij} + m_i(\mathbf{v}'_i)(\mathbf{v}'_i)\right] \tag{4}$$

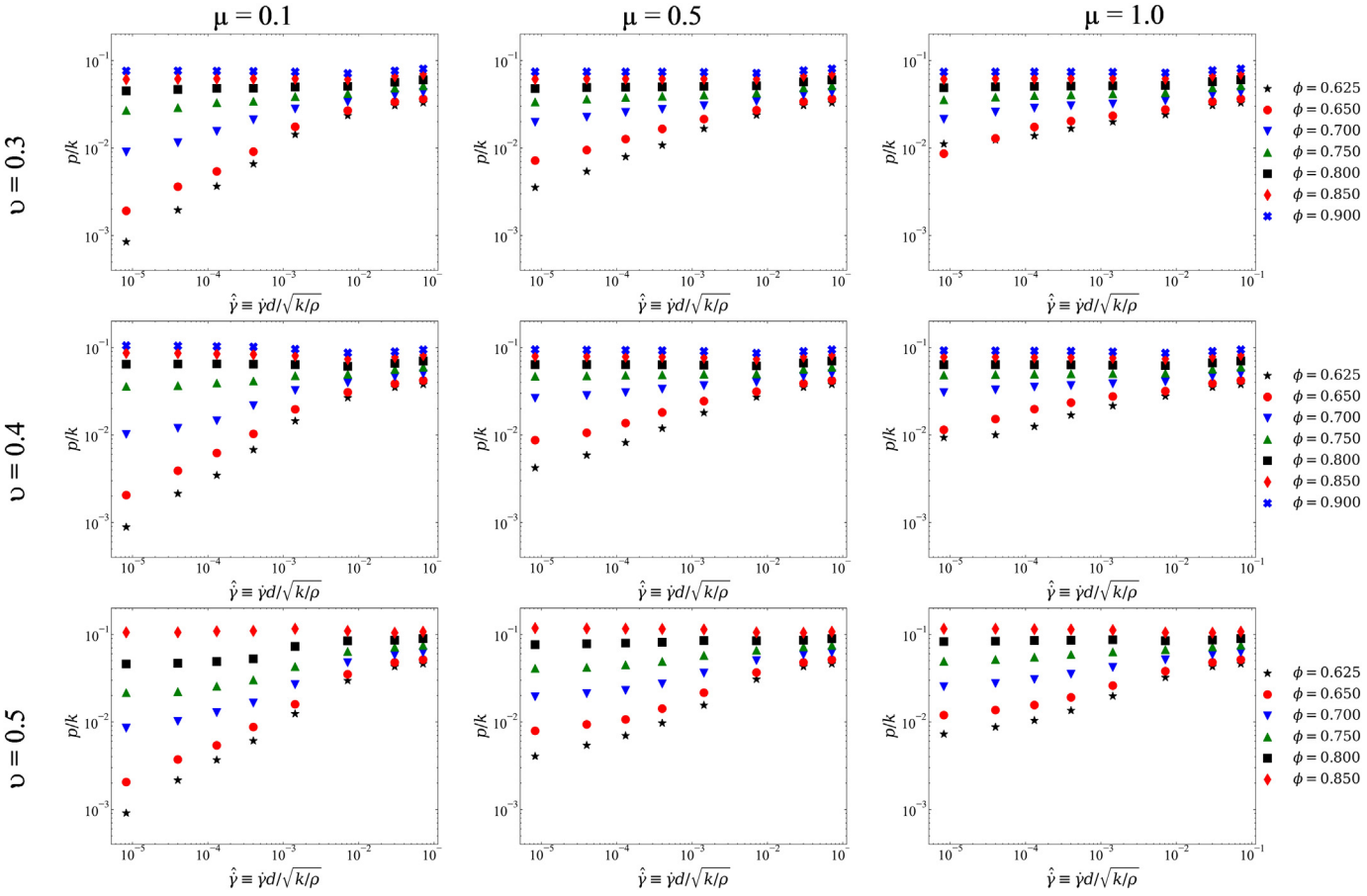

Fig. 8. Dimensionless pressure vs. dimensionless shear rate for different combinations of particle-particle friction coefficients and Poisson's ratio using advanced MC-DEM.

Here V is the volume of the simulation box, $\mathbf{r}_{ij}$ is the center-to-center vector from particle j to i, and $\mathbf{v}'_i$ is the particle velocity relative to the local mean particle velocity. The packing's average pressure is calculated as $p = (\sigma_{xx} + \sigma_{yy} + \sigma_{zz})/3$. This value is made dimensionless with the normal stiffness of the particles by deploying the Hertzian contact law. The normal and tangential contact forces are calculated as:

$$\mathbf{F}_{nij} = \sqrt{\delta_{ij} R_{eff}}\left[k_n \delta_{ij} \mathbf{n}_{ij} - \gamma_n m_{eff} \mathbf{v}_{nij}\right] \tag{5}$$

$$\mathbf{F}_{tij} = \sqrt{\delta_{ij} R_{eff}}\left[-k_t \mathbf{u}_{tij} - \gamma_t m_{eff} \mathbf{v}_{tij}\right] \tag{6}$$

Here, δ_{ij} is the overlap distance which is calculated from Eq. 3, $R_{eff} = R_i R_j/(R_i + R_j)$ is the effective radius of two contacting particles i and j, k_n and k_t are the normal and tangential stiffness constants, γ_n and γ_t are the viscous damping constants, $m_{eff} = m_i m_j/(m_i + m_j)$ is the effective mass for particle masses m_i and m_j, $\mathbf{v}_{nij}$ and $\mathbf{v}_{tij}$ are relative particle velocity in normal and tangential directions, and $\mathbf{u}_{tij}$ is the elastic shear displacement, which is truncated to fulfill the static yield criterion, $|\mathbf{F}_{tij}| \le \mu|\mathbf{F}_{nij}|$, where μ is the particle friction coefficient. The explicit calculation of the stiffness and viscous damping constants are reported in Appendix C.

The shear rate has been also made dimensionless with the following relation

$$\hat{\dot{\gamma}} \equiv \dot{\gamma}\, d/\sqrt{k_n/\rho} \tag{7}$$

where ρ is the particle density.

4.2. Results and discussion

Three main flow regimes are observed in simple shear flow. These regimes are bounded by the critical volume fraction, ϕ_c, corresponding to the jamming condition. A collisional/inertial regime (below ϕ_c) exists where the spheres interact through collisions that can be regarded as instantaneous, binary, and uncorrelated. The pressure is quadratic in the shear rate in this regime. A deformational/quasi-static regime is present at volume fractions larger than ϕ_c. The pressure is shear rate independent in this regime. As the shear rate increases, the quasi-static and inertial regime reach a common asymptote independent of the volume fraction of the system. This regime is referred to as the intermediate regime.

The current study focuses on the key parameters in the shear flow of soft particles above the jamming point. Preliminary simulations confirmed that the coefficient of restitution did not affect the stress response for all systems studied. Thus, the normalized stress is primarily a function of the coefficient of friction, the particle volume fraction, and the dimensionless shear rate. Interestingly, we find an additional effect of the Poisson's ratio, which can only be identified when using a MC contact force closure. Note that in simple shear flow simulations that use the classical Hertz contact law, the effect of the Poisson's ratio is negligibly small (Fig. 7).

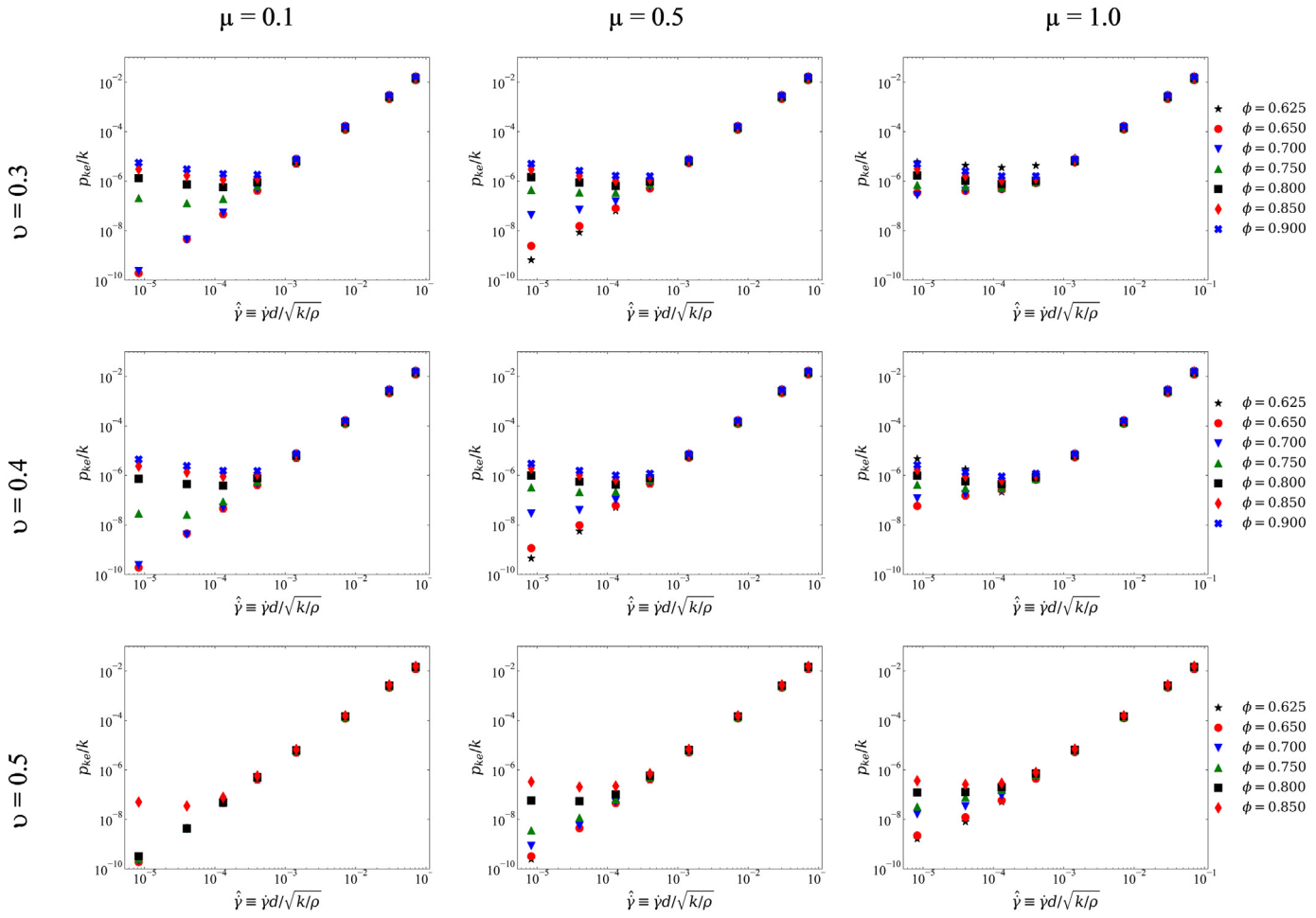

Fig. 9. Dimensionless kinetic pressure vs. dimensionless shear rate for different combinations of particle-particle friction coefficients and Poisson's ratio using advanced MC-DEM.

The simulations were carried out for $\mu = 0.0, 0.1, 0.3, 0.5$ and 1.0, as well as for Poisson's ratios between $\upsilon = 0.25$ and 0.50. Fig. 8 shows the evolution of dimensionless pressure with the dimensionless shear rate for selected Poisson's ratio and friction coefficients. As it was expected [32], the overall quasi-static pressure increases up to one order of magnitude when increasing the friction coefficient for $\phi < 0.75$ (see Fig. 8). This behavior is observed because the critical solid volume fraction is dependent on the friction coefficient. Generally, for $\phi > 0.7$ the curves from all shear rates collapse to one, as the frictional particles become more deformable (higher dimensionless shear rate) as if the granular system becomes an elastic solid. This is less significant for incompressible particles (i.e., $\upsilon = 0.5$), owing to the generation of larger lateral particle deformation. Our results confirm previous observations [32] of the distinguishable regime transitions for higher friction coefficients. At lower shear rates, the shear stress becomes highly dependent on the friction coefficient. Comparing $\phi = 0.625$ and 0.65, for $\mu = 1.0$ (particularly at lower shear rates), shows the significant effect of the larger inter-particle overlaps with higher Poisson's ratio, leading to divergent points.

As shown in Fig. 9, the order of magnitude of the dimensionless kinetic pressure is negligible compared to the ensemble-averaged contact pressure (i.e., the first term in Eq. 4). This behavior is expected for jammed sheared packings. Interestingly, it has been found that for the softer particles (or higher dimensionless shear rates), the kinetic pressure is independent of the solid volume fraction and increases linearly with the increase of $\hat{\dot{\gamma}}$. Also, as friction increases, the dimensionless kinetic pressure reaches a common plateau at low $\hat{\dot{\gamma}}$. Moreover, the kinetic pressure becomes more dependent on the solid volume fraction for lower friction coefficients and as particles get stiffer (i.e., $\hat{\dot{\gamma}}$ is reduced).

One of the quantities that can show the arrangement of the particles and their behavior under jammed conditions is the ensemble-average coordination number Z. We define this value for each particle i as $Z_i = 2N_c/N$, where N_c is the number of contacts per particle for an N-particle assembly. Since the values of ensemble-averaged Z do not significantly fluctuate in the quasi-static regime, they are securely time-averaged. Thus, in what follows only means are reported as already done for the stress. As displayed in Fig. 10, the time-averaged Z values monotonically decrease when increasing $\hat{\dot{\gamma}}$, and reach a plateau for high dimensionless shear rates. The difference between the higher and lower coordination numbers for each solid volume fraction becomes more significant as particles get smoother (i.e., the friction coefficient decreases) and the Poisson's ratio drops.

4.3. Response surface of quasi-static pressure model for deformable particles

Both experimental [33] and computational [32] studies of shear flows above the jamming point have proven that the pressure data can be collapsed on a curve by powers of the distance to a critical particle volume fraction $|\phi - \phi_c|$. Thus, the pressure in the quasi-static regime can be modeled as:

$$p_{QS}/k = \alpha_{QS}|\phi - \phi_c|^{\beta} \tag{8}$$

It is argued that α_{QS} is a friction coefficient-dependent, and β is a contact model-dependent parameter [34]. The results of the advanced multi-contact indicated that the stress is dependent on both the friction and the Poisson's ratio (see Fig. 11), especially for highly dense packings.

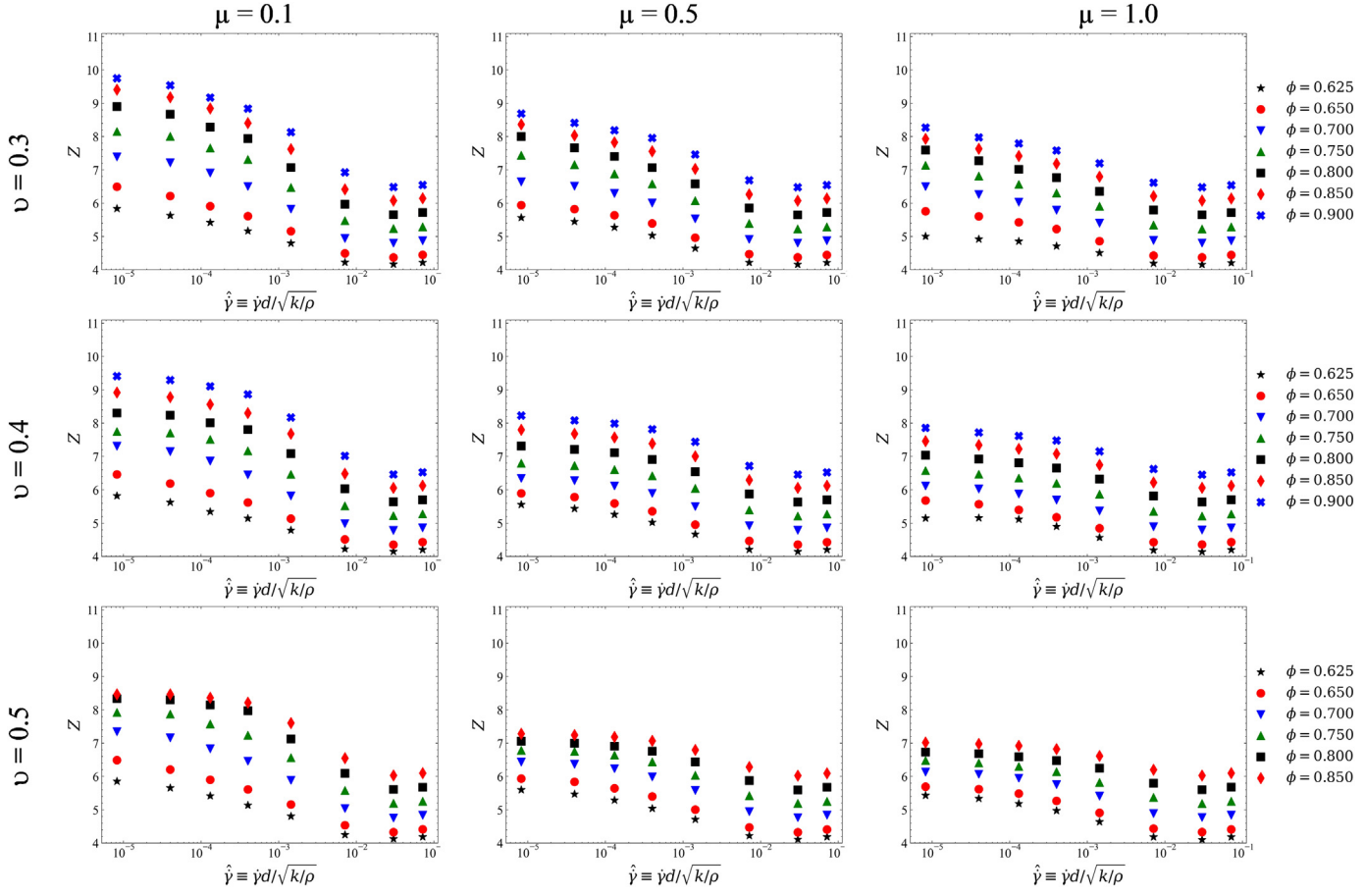

Fig. 10. Average coordination number vs. dimensionless shear rate for various solid volume fractions and friction coefficients using advanced MC-DEM.

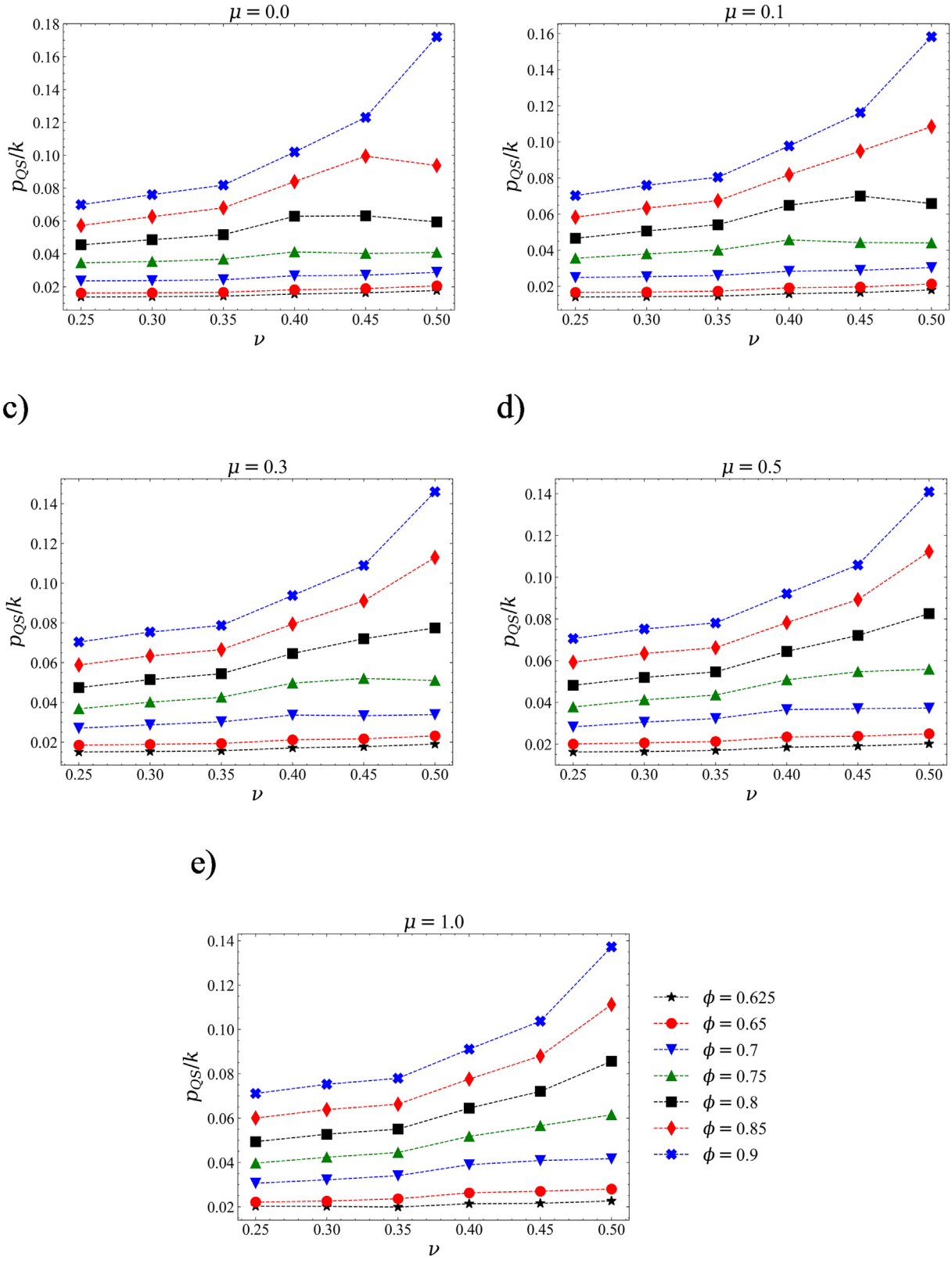

Fig. 11. Averaged quasi-static pressure versus the Poisson's ratio for different friction coefficients.

Hence, the same holds for the parameters in Eq. 8. It is observed that the effect of the Poisson's ratio becomes more significant as the particles become frictionless, as the quasi-static pressure only consists of static contribution from the elasticity of the particles, while with frictional particles similes gels with higher viscosity, leading to lower pressure predictions. Since this behavior is complex, the evolution of these pressure model parameters with various friction coefficients and Poisson's ratios is depicted in Fig. 12.

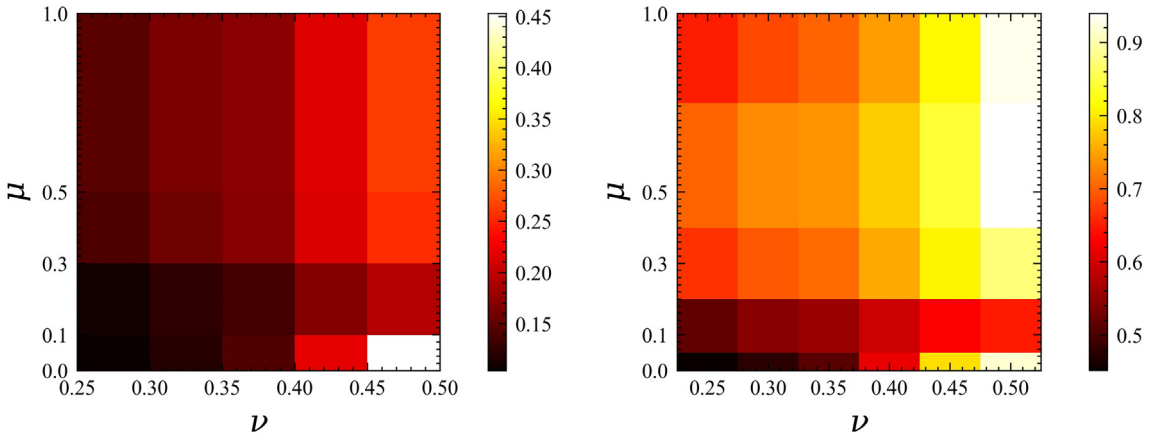

Fig. 12. The evolution of the quasi-static pressure model (a) slope α_{QS} and (b) the exponent β for various friction coefficients and Poisson's ratios. (For the exact values, see Appendix D).

5. Conclusion

An existing contact force closure for extremely dense granular flows, the standard multi-contact (MC) closure proposed by Brodu et al. [21], was improved and parameters calibrated. Specifically, we propose to introduce a maximum penetration ratio at which one should switch between the formulation of Brodu et al. [21] and the classical Hertzian contact force closure. As a result, our advanced MC closure can now reliably model dense configurations of particles where conventional models (e.g., Hertzian contact laws or standard MC) are inaccurate or numerically unstable.

Our advanced MC model enables DEM-based simulations of granular flows characterized by solid volume fractions greater than 0.7. This was demonstrated for monodisperse particle packings for uniaxial compression and simple shear flow. Our model has been verified by comparing the results with an accurate reference model (i.e., a nonlocal formulation of particle deformation). The results showed that as soft particles become more incompressible (i.e., υ approaches 0.5), a calibration approach that considers a variety of the Young's moduli should be followed. Finally, it was shown that the optimal geometric pre-factor in our advanced MC model is linearly dependent on the Poisson's ratio.

The key influence parameters on the stress in the simple shear flow of soft particles above the jamming point were closely investigated. This is particularly valuable for calibrating model parameters, specifically if advanced multi-contact DEM models are used. Although it has been shown in previous studies that the only key parameter affecting the quasi-static pressure is the coefficient of friction, our present analysis showed that the Poisson's ratio also plays a key role.

Future work could explore if our model predictions are in line with reference data for bi-disperse or poly-disperse material. The effect of large inter-particle friction coefficients on the parameter calibration of the advanced MC method should be investigated. Also, it has to be noted that the full extent of the model's validity should be assessed by careful comparison with experimental data, possibly requiring an additional calibration step.

Nomenclature

Symbol	Property, Units
d	*Particle's diameter, m*
d_{kc}	*Distance between surface position of contacts c and k, m*
E	*Young's modulus, Pa*
$\mathbf{F}_{ij}$	*Contact force between particle i and j, N*
$\mathbf{F}_k$	*Force at contact k, N*
k (k_n)	*Particle's normal stiffness, N/m²*
k_t	*Particle's tangential stiffness, N/m²*
m_i	*Mass of particle i, kg*
m_{eff}	*Effective mass of two contacting particles i and j, kg*
$\mathbf{n}_c$	*Surface normal unit vector at contact c, –*
$\mathbf{n}_k$	*Surface normal unit vector at contact k, –*
N	*Total number of particles, –*
N_c	*Number of contacts per particle, –*
R_{eff}	*Effective radius of two contacting particles i and j, m*
R_i	*Radius of particle i, m*
r_{ij}	*Center-to-center vector form particle j to i, m*
p	*Packing's averaged pressure, Pa*
p_{ke}	*Packing's averaged kinetic pressure, Pa*
p_{QS}	*Packing's averaged pressure in quasi-static state, Pa*
$\mathbf{u}_{kc}$	*Unit vector from contact k to c, –*
V	*Volume of the simulation box, m³*
Z	*Coordination number, –*
α_{QS}	*The coefficient in quasi-static pressure model, –*
β	*The exponent in the quasi-static pressure model, –*
γ	*Empirical geometric pre-factor, –*
$\dot{\gamma}$	*Shear rate, 1/s*
$\dot{\gamma}$	*Dimensionless shear rate, –*
γ_n	*Normal viscous damping constant, 1/m.s*
γ_t	*Tangential viscous damping constant, 1/m.s*
δ_{ij}	*Overlap distance between two contacting particles i and j, m*
δ_c	*Displacement field at local contact c, m*
$\delta_{k\to c}$	*Displacement field by neighboring contacts, m*
δ_{max}	*Maximum displacement per contact, m*
μ	*Coefficient of friction, –*
υ	*Poison's ratio, –*
ρ	*Particle's density, kg/m³*
σ	*Macroscopic stress tensor, Pa*
ϕ	*Solid volume fraction, –*
ϕ_c	*Critical solid volume fraction, –*
$\mathbf{v}'_i$	*Particle velocity relative to its mean velocity, m/s*

CRediT authorship contribution statement

Nazanin Ghods: Conceptualization, Methodology, Software, Writing – original draft, Visualization. **Payam Poorsolhjouy:** Validation, Formal analysis, Writing – original draft. **Marcial Gonzalez:** Writing – review & editing, Formal analysis. **Stefan Radl:** Conceptualization, Writing – review & editing, Supervision, Project administration.

Declaration of Competing Interest

The authors declare that they have no known competing financial interests or personal relationships that could have appeared to influence the work reported in this paper.

Acknowledgment

TU Graz researchers acknowledge discussions with Arno Mayrhofer at DCS Computing on implementation details of the original multi-contact force closure and fruitful discussions with Mohammadsadegh Salehi for assessing the shortcomings of the standard multi-contact closure. Financial support by the European Union's Horizon 2020 Marie Skłodowska-Curie grant 'CALIPER' (No. 812638), and by NAWI Graz (via access to its HPC computing resource dcluster.tugraz.at) is acknowledged by TU Graz researchers. Poorsolhjouy gratefully acknowledges the financial support provided by Sectorplan Techniek, Netherlands.

Appendix A. Advanced MC-DEM algorithm

The following algorithm shows how the advanced multi-contact method calculates the contact forces based on the local deformation.

```
loop over all particles:
loop over all contacts of particle i:
compute the surface position of contact ij and ji
get the normal force on the particle
loop over all contacts ij
loop over all other contacts of particle i
temp_delta = calculated displacement from Eq. 2
if temp_delta > mpr then: delta = 0.0
else: delta_i = delta_i + temp_delta
radius_i = radius_i + delta_i

continue general DEM force calculation with the deformed particles (new radii)
reset the particles' radii to their original value for the next time step
```

Table 1
Hydrogel particle properties for the compression tests [21].

Material Properties	Effective Density* (kg/m^3)	Young's Modulus (Pa)	Poisson's ratio	Restitution coefficient	Friction coefficient
Values	11.5	23.3×10^3	0.5	0.95	0.03

* Effective density means the density of particles minus the density of the ambient fluid (water).

Appendix B. Modeling test cases with hydrogel particle (verification of microstructural features)

Two test cases were examined to verify the microstructural features of the advanced multi-contact closure on the particle level. In both cases, hydrogel particles with a diameter of 2 mm, and properties reported in Table 1 were utilized. In the first test case, a single particle, and in the other test case, nine particles with bcc (body-centered cubic) arrangement, enclosed in a rigid box, are compressed with constant velocity (0.01 m/s) from above (see Fig. B.1). The applied stress on the compression plate and the lateral stress exerted on the side walls have been studied with Hertz, MC, and advanced MC models (see Fig. B.2).

A perfect agreement between the reference nonlocal formulation and the multi-contact models is observed by choosing $\gamma = 0.82$ for the standard MC, and $\gamma = 0.81$ and an MPR value of 0.11 for the advanced MC closure. The MC and Advanced MC responses are entirely consistent in these two cases due to the low coordination number

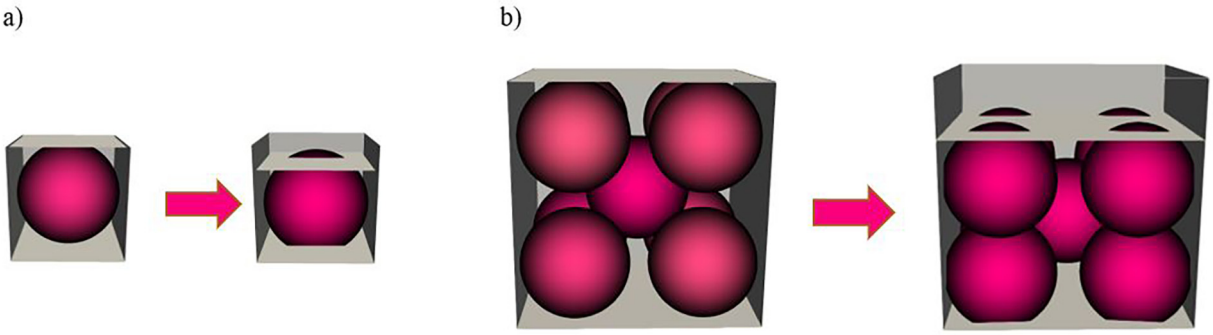

Fig. B.1. Schematic representation of a) a single hydrogel particle b) a bcc structure of nine identical hydrogel particles, compressed in a rigid box, with $E = 5.0 \times 10^7$, assuming a friction coefficient of 0.03 for particle-wall interactions.

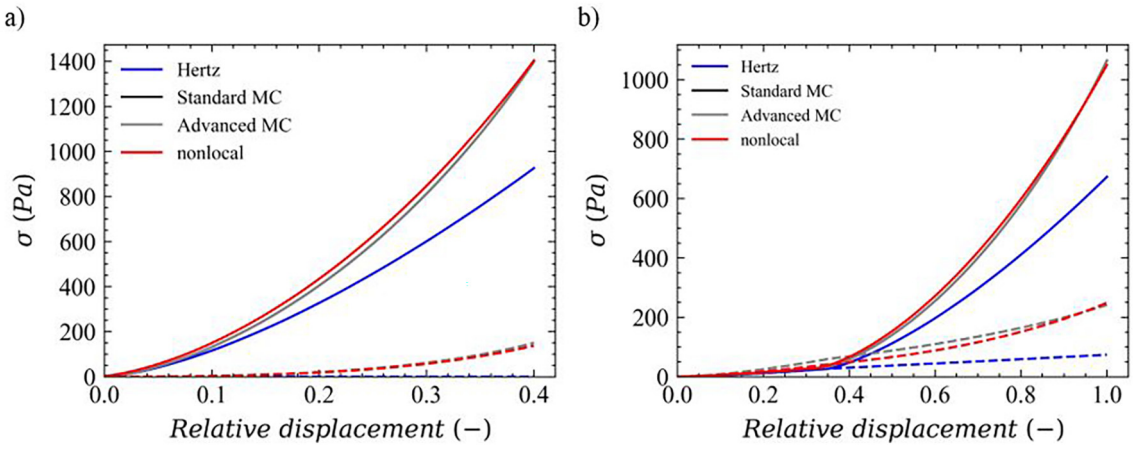

Fig. B.2. Stress-displacement response of a) a single hydrogel particle, and b) a bcc structure of nine identical hydrogel particles during compression. Relative displacement is defined as the plate displacement divided by particle's radius. The solid lines show the stress on the compressing plate, and the dashed lines show the lateral stress on sidewalls.

and compression level. Consideration of the lateral stress shows an adequate consideration of particle deformation in the MC models. Also, the lateral stress predicted with the conventional DEM using the Hertz contact law in the bcc structure is non-zero. This is due to the component of the contact forces oriented in the direction perpendicular to the compression direction. However, the Hertz contact law significantly underpredicts the lateral stress compared to results of all other models.

Appendix C. Parameter definition of Hertz contact model parameters

Here follows a series of definitions showing how the parameters defined in eqs. 5 and 6 are related to the material properties of two contacting particles *i* and *j*, when using the Hertz contact model:

$$k_n = \frac{4}{3}E^*, \tag{C.1}$$

$$\gamma_n = -2\sqrt{\frac{5}{6}}\beta\sqrt{S_n m_{eff}} \tag{C.2}$$

where

$$\frac{1}{E^*} = \frac{(1-\upsilon_i^2)}{E_i} + \frac{\left(1-\upsilon_j^2\right)}{E_j}, \tag{C.3}$$

$$\beta = \frac{ln\,(e)}{ln^2(e)+\pi^2}, \tag{C.4}$$

$$S_n = \frac{2E^*}{\sqrt{R_{eff}\delta_{ij}}} \tag{C.5}$$

where *e* is the particle's restitution coefficient.

And for the tangential properties we have:

$$k_t = 8G^*, \tag{C.6}$$

$$\gamma_t = -2\sqrt{\frac{5}{6}}\beta\sqrt{S_t m_{eff}} \tag{C.7}$$

where

$$\frac{1}{G^*} = \frac{2(2-\upsilon_i)(1+\upsilon_i)}{E_i} + \frac{2(2-\upsilon_j)(1+\upsilon_j)}{E_j}, \tag{C.8}$$

$$S_t = \frac{8G^*}{\sqrt{R_{eff}\delta_{ij}}} \tag{C.9}$$

Appendix D. Quasi-static pressure model parameters

The exact values of the maps shown in Fig. 12, is reported in the bellowed tables:

Table D.1
The slope α_{QS} values of the quasi-static pressure model (Eq. 8) for various friction coefficients and Poisson's ratios.

		Poisson's ratio					
		0.25	0.30	0.35	0.40	0.45	0.50
Friction Coefficient	0.0	0.104277	0.118771	0.141813	0.21954	0.453046	0.916128
	0.1	0.110574	0.123689	0.133818	0.167847	0.193596	0.221763
	0.3	0.139061	0.156818	0.168427	0.212168	0.25459	0.325325
	0.5	0.145432	0.163232	0.172328	0.215745	0.262769	0.358336
	1.0	0.135648	0.151223	0.162276	0.201806	0.247903	0.354467

Table D.2
The exponent β values of the quasi-static pressure model (Eq. 8) for various friction coefficients and Poisson's ratios.

		Poisson's ratio					
		0.25	0.30	0.35	0.40	0.45	0.50
Friction Coefficient	0.0	0.451572	0.47525	0.509283	0.615447	0.7912	0.916196
	0.1	0.516353	0.543197	0.556984	0.594151	0.62764	0.649442
	0.3	0.666142	0.695518	0.708862	0.752943	0.806323	0.874100
	0.5	0.702005	0.730395	0.735797	0.779424	0.840925	0.939593
	1.0	0.650966	0.683512	0.701467	0.744274	0.810227	0.929334

References

[1] P. Cundall, O. S.- geotechnique, and undefined, A discrete numerical model for granular assemblies, *icevirtuallibrary.com* 1979 , Accessed: Mar. 22, 2021. [Online]. Available https://www.icevirtuallibrary.com/doi/abs/10.1680/geot.1979.29.1.47.

[2] M. Gonzalez, A.M. Cuitiño, A nonlocal contact formulation for confined granular systems, J. Mech. Phys. Solids 60 (2) (Feb.2012) 333–350, https://doi.org/10.1016/j.jmps.2011.10.004.

[3] L. Orefice, J.G. Khinast, Deformable and breakable DEM particle clusters for modelling compression of plastic and brittle porous materials — model and structure properties, Powder Technol. (2020) https://doi.org/10.1016/j.powtec.2020.04.035.

[4] J. Wang, et al., Silo discharge of mixtures of soft and rigid grains, Soft Matter (2021) https://doi.org/10.1039/d0sm01887b.

[5] D.A. Fedosov, H. Noguchi, G. Gompper, Multiscale modeling of blood flow: from single cells to blood rheology, Biomech. Model. Mechanobiol. (2014) https://doi.org/10.1007/s10237-013-0497-9.

[6] J.P. Plassiard, N. Belheine, F.V. Donzé, A spherical discrete element model: Calibration procedure and incremental response, Granul. Matter 11 (5) (2009) 293–306, https://doi.org/10.1007/s10035-009-0130-x.

[7] C.L. Martin, D. Bouvard, S. Shima, Study of particle rearrangement during powder compaction by the discrete element method, J. Mech. Phys. Solids (2003) https://doi.org/10.1016/S0022-5096(02)00101-1.

[8] D. Suzzi, et al., DEM simulation of continuous tablet coating: effects of tablet shape and fill level on inter-tablet coating variability, Chem. Eng. Sci. (2012) https://doi.org/10.1016/j.ces.2011.10.009.

[9] J. Härtl, J.Y. Ooi, Numerical investigation of particle shape and particle friction on limiting bulk friction in direct shear tests and comparison with experiments, Powder Technol. 212 (1) (2011) 231–239, https://doi.org/10.1016/j.powtec.2011.05.022.

[10] I.J. Stránský, Mesoscale Discrete Element Model for Concrete and its Combination with FEM, 2018.

[11] A. Mazor, L. Orefice, A. Michrafy, A. de Ryck, J.G. Khinast, A combined DEM & FEM approach for modelling roll compaction process, Powder Technol. (2018) https://doi.org/10.1016/j.powtec.2017.04.053.

[12] G. Frenning, An efficient finite/discrete element procedure for simulating compression of 3D particle assemblies, Comput. Methods Appl. Mech. Eng. (2008) https://doi.org/10.1016/j.cma.2008.05.002.

[13] D.T. Gethin, R.W. Lewis, R.S. Ransing, A discrete deformable element approach for the compaction of powder systems, Model. Simul. Mater. Sci. Eng. (2003) https://doi.org/10.1088/0965-0393/11/1/308.

[14] P. Loidolt, M.H. Ulz, J. Khinast, Prediction of the anisotropic mechanical properties of compacted powders, Powder Technol. (2019) https://doi.org/10.1016/j.powtec.2019.01.048.

[15] T. Lo Vu, S. Nezamabadi, J. Barés, S. Mora, Analysis of Dense Packing of Highly Deformed Grains, 2017 https://doi.org/10.1051/epjconf/201714015031.

[16] S. Mora, T. Lo Vu, J. Barés, S. Nezamabadi, Highly Deformed Grain: From the Hertz Contact Limitation to a New Strain Field Description in 2D, 2017 https://doi.org/10.1051/epjconf/201714005011.

[17] I. Iaconeta, A. Larese, R. Rossi, E. Oñate, An Implicit Material Point Method Applied to Granular Flows, 2017 https://doi.org/10.1016/j.proeng.2017.01.017.

[18] M. Dosta, C. Costa, H. Al-Qureshi, Numerical Investigation of Compaction of Deformable Particles with Bonded-Particle Model, 2017 https://doi.org/10.1051/epjconf/201714015021.

[19] J. Rojek, A. Zubelewicz, N. Madan, S. Nosewicz, The discrete element method with deformable particles, Int. J. Numer. Methods Eng. 114 (8) (2018) 828–860, https://doi.org/10.1002/nme.5767.

[20] G. Hua Shi, Discontinuous deformation analysis: a new numerical model for the statics and dynamics of deformable block structures, Eng. Comput. (1992) https://doi.org/10.1108/eb023855.

[21] N. Brodu, J.A. Dijksman, R.P. Behringer, Multiple-contact discrete-element model for simulating dense granular media, Phys. Rev. E - Stat. Nonlinear, Soft Matter Phys. 91 (3) (2015) https://doi.org/10.1103/PhysRevE.91.032201.

[22] K. Giannis, et al., Stress based multi-contact model for discrete-element simulations, Granul. Matter 23 (2) (2021) https://doi.org/10.1007/s10035-020-01060-8.

[23] P. Poorsolhjouy, M. Gonzalez, Connecting discrete particle mechanics to continuum granular micromechanics: anisotropic continuum properties under compaction, arXiv 92 (2018) 21–27.

[24] A. Agarwal, M. Gonzalez, Contact radius and curvature corrections to the nonlocal contact formulation accounting for multi-particle interactions in elastic confined

granular systems, Int. J. Eng. Sci. 133 (2018) 26–46, https://doi.org/10.1016/j.ijengsci.2018.08.006.
[25] C. Kloss, C. Goniva, A. Hager, S. Amberger, S. Pirker, Models, algorithms and validation for opensource DEM and CFD-DEM, Prog. Comput. Fluid Dyn. 12 (2–3) (2012) 140–152, https://doi.org/10.1504/PCFD.2012.047457.
[26] C. O'Sullivan, J.D. Bray, Selecting a suitable time step for discrete element simulations that use the central difference time integration scheme, Eng. Comput. (Swansea, Wales) 21 (2–4) (2004) 278–303, https://doi.org/10.1108/02644400410519794.
[27] S. Mukhopadhyay, J. Peixinho, Packings of deformable spheres, Phys. Rev. E - Stat. Nonlinear, Soft Matter Phys. (2011) https://doi.org/10.1103/PhysRevE.84.011302.
[28] J.D. James, J.M. Ludwick, M.L. Wheeler, M.L. Oyen, Compressive failure of hydrogel spheres, J. Mater. Res. (2020) https://doi.org/10.1557/jmr.2020.114.
[29] Y. Tatara, S. Shima, J.C. Lucero, On compression of rubber elastic sphere over a large range of displacements-part 2: comparison of theory and experiment, J. Eng. Mater. Technol. Trans. ASME (1991) https://doi.org/10.1115/1.2903408.
[30] S. Shima, Y. Tatara, M. Iio, C. Shu, J.C. Lucero, Large deformations of a rubber sphere under diametral compression. (Part 2: Experiments on many rubber materials and comparisons of theories with experiments), JSME Int. Journal, Ser. A Mech. Mater. Eng. (1993) https://doi.org/10.1299/jsmea1993.36.2_197.
[31] A.W. Lees, S.F. Edwards, The computer study of transport processes under extreme conditions, J. Phys. C Solid State Phys. 5 (15) (1972) 1921–1928, https://doi.org/10.1088/0022-3719/5/15/006.
[32] S. Chialvo, J. Sun, S. Sundaresan, Bridging the rheology of granular flows in three regimes, Phys. Rev. E - Stat. Nonlinear, Soft Matter Phys. 85 (2) (2012) 1–8, https://doi.org/10.1103/PhysRevE.85.021305.
[33] K.N. Nordstrom, et al., Microfluidic rheology of soft colloids above and below jamming, Phys. Rev. Lett. 105 (17) (2010) 1–4, https://doi.org/10.1103/PhysRevLett.105.175701.
[34] T. Hatano, Scaling properties of granular rheology near the jamming transition, J. Phys. Soc. Jpn. 77 (12) (2008) 18–21, https://doi.org/10.1143/JPSJ.77.123002.